computation

MDPI

Article

Development and Assessment of Simplified Conductance Models for the Particle Exhaust in Wendelstein 7-X

Foteini Litovoli [1,*], Christos Tantos [1], Volker Hauer [1], Victoria Haak [2], Dirk Naujoks [2], Chandra-Prakash Dhard [2] and W7-X Team [†]

[1] Institute for Technical Physics, Karlsruhe Institute of Technology, 76344 Eggenstein-Leopoldshafen, Germany; christos.tantos@kit.edu (C.T.); volker.hauer@kit.edu (V.H.)
[2] Max-Planck Institute for Plasma Physics, Wendelsteinstrasse 1, 17491 Greifswald, Germany; victoria.haak@ipp.mpg.de (V.H.); dirk.naujoks@ipp.mpg.de (D.N.); chandra.prakash.dhard@ipp.mpg.de (C.-P.D.)
* Correspondence: foteini.litovoli@kit.edu; Tel.: +49-721-608-29169
† Collaborators/Membership of the W7-X Team is provided in the Acknowledgments.

Abstract

The particle exhaust system plays a pivotal role in fusion reactors and is essential for ensuring both the feasibility and sustained operation of the fusion reaction. For the successful development of such a system, density control is of great importance and some key design parameters include the neutral gas pressure and the resulting particle fluxes. This study presents a simplified conductance-based model for estimating neutral gas pressure distributions in the particle exhaust system of fusion reactors, focusing specifically on the sub-divertor region. In the proposed model, the pumping region is represented as an interconnected set of reservoirs and channels. Mass conservation and conductance relations, appropriate for all flow regimes, are applied. The model was benchmarked against complex 3D DIVGAS simulations across representative operating scenarios of the Wendelstein 7-X (W7-X) stellarator. Despite geometric simplifications, the model is capable of predicting pressure values at several key locations inside the particle exhaust area of W7-X, as well as various types of particle fluxes. The developed model is computationally efficient for large-scale parametric studies, exhibiting an average deviation of approximately 20%, which indicates reasonable predictive accuracy considering the model simplifications and the flow problem complexity. Its application may assist early-stage engineering design, pumping performance improvement, and operational planning for W7-X and other future fusion reactors.

Keywords: fusion technology; particle exhaust system; conductance; W7-X

Check for updates

Academic Editors: Ali Cemal Benim, Jeffrey S. Marshall, Sergey A. Karabasov and Dimitris Drikakis

Received: 15 December 2025
Revised: 11 January 2026
Accepted: 15 January 2026
Published: 19 January 2026

Copyright: © 2026 by the authors. Licensee MDPI, Basel, Switzerland. This article is an open access article distributed under the terms and conditions of the Creative Commons Attribution (CC BY) license.

1. Introduction

Fusion energy is rapidly becoming an important topic in the worldwide industry. It is considered a promising solution for long-term sustainable energy production. In recent years, research activity around magnetic confinement fusion has increased significantly. Various designs are being explored, from conventional tokamaks [1–4] to more complex stellarator systems [5–7]. A standout example in this category is Wendelstein 7-X (W7-X) [8,9], one of the most advanced stellarator projects in operation today, hosted by the Max Planck Institute for Plasma Physics (IPP) in Greifswald, Germany.

The divertor is an important subsystem of the particle exhaust in any large or small fusion reactor. The divertor design must meet multiple requirements, including neutron

shielding, efficient heat removal, and effective particle exhaust. Reliable modeling of divertor behavior is essential for predicting operational limits and designing reactor-scale devices. As plasma pulses become longer and higher in performance, the development of accurate and computationally efficient divertor modeling tools is becoming more critical. Modeling the divertor region presents significant challenges due to its complex geometry and the wide range of gas flow regimes encountered very often in the particle exhaust area of fusion machines. Depending on the device size and operating conditions, the neutral gas dynamics can span the full spectrum of rarefaction. As a result, accurately describing this behavior requires solving the Boltzmann equation, an inherently complex task that can only be addressed using computationally intensive numerical methods such as Direct Simulation Monte Carlo (DSMC) [10] and the Discrete Velocity Method (DVM) [11].

At the Karlsruhe Institute of Technology (KIT), the Divertor Gas Simulator (DIVGAS) has been developed to simulate 2D/3D multispecies gas flows in the divertor and sub-divertor regions of tokamaks and stellarators. DIVGAS is a powerful computational workflow based on DSMC and DVM, providing detailed analysis of neutral gas dynamics inside the particle exhaust area of fusion reactors. It has been successfully applied to devices such as W7-X [12], DTT [13,14], DEMO [15,16], and others, especially in designing and validating particle exhaust and pumping systems, and has been validated with experimental results [17,18].

Neutral transport in divertor and sub-divertor regions has been widely studied, with previous works focusing on empirical scaling, 2D modeling, or 3D simulations of neutral pressures and fluxes [12–16,19,20]. However, due to the 3D complexity of divertor geometries and the high computational cost of such simulations, there is strong motivation to develop simplified models that can provide fast and physically meaningful estimates of pressure distributions in exhaust systems [21,22]. These models typically represent the volume as a combination of channels and reservoirs. In [22], their accuracy was evaluated by comparison with experimental results from a single linear plasma device. The formulation based on interconnected reservoirs, conductance relations, and mass-balance equations is a well-established and long-standing approach in vacuum network modeling [23–26]. The goal of our manuscript is to provide a simplified and application-oriented model specifically adapted to the W7-X divertor configuration, while drawing upon the broad methodological heritage of conductance-based vacuum system analysis. The applied model is based on the mass conservation principle and represents the sub-divertor pumping area as a collection of interconnected reservoirs linked by channels. The behavior of models with two-, three-, and four-reservoir representations is studied, and the validity of the model is examined against numerical data for pressure and particle fluxes obtained from 3D DIVGAS simulations [12].

2. Conductance Model for W7-X Sub-Divertor

In this work, the sub-divertor is modeled using a simplified arrangement of reservoirs and connecting channels, representing selected areas of interest while avoiding the complexity of a full-scale model [12,18]. The channels are characterized by their individual gas conductance, which quantify the ease with which the gas can flow between the different regions. Each reservoir corresponds to a localized region where the gas pressure is assumed to be approximately uniform. The model applies the principle of mass conservation to establish relationships between pressures and flow rates throughout the entire network. The presentation of the proposed model is organized into the following three subsections. Section 2.1 describes the simplification of the W7-X sub-divertor geometry into reservoirs and connecting channels. In Section 2.2, the formulation of the 2-, 3-, and 4-reservoir models based on mass conservation is introduced. This is followed by the applied through-

put and conductance relations, presented in Sections 2.3 and 2.4, respectively, which are incorporated into the model equations.

2.1. W7-X Geometry Simplification

Figure 1 provides an overview of one of the divertor units of W7-X. Each divertor unit can be divided into two main parts, the low-iota (AEH) and high-iota (AEP) sections. The low iota section includes the horizontal and vertical target elements and the large pumping gap on the inboard side. In the high iota section, the small pumping gap is located on the outboard side next to the horizontal target elements. In total, there are 10 divertor units in W7-X.

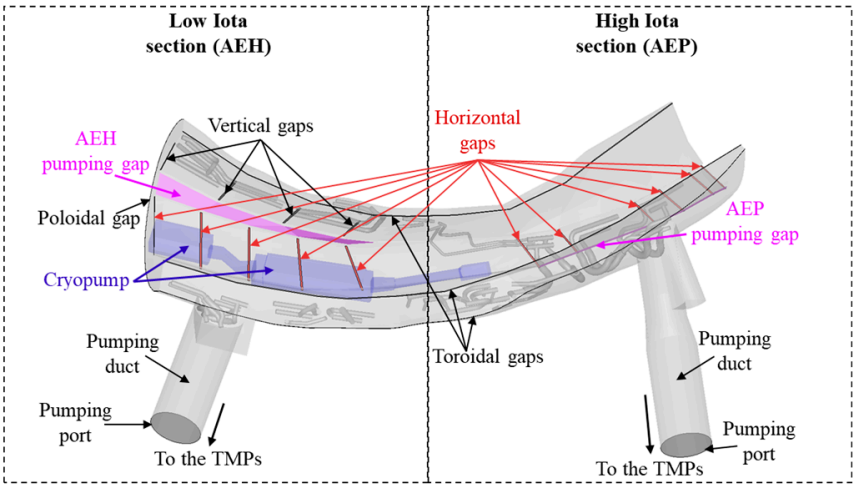

Figure 1. The sub-divertor of W7-X, showing the AEH and AEP pumping sections, the location of the turbomolecular pumps and cryopump, and the leakage openings.

The divertor unit is equipped with turbomolecular pumps (TMPs), positioned at the AEH and AEP sections following the pumping ports, and with a cryopump (CVP), which lies beneath the AEH horizontal target modules. Specifically, the cryopump consists of two modules, referred to as the big and small modules according to their size. Further details on the TMPs and CVP can be found in Ref. [27]. The neutral gas particles enter the W7-X sub-divertor area through the AEH and AEP pumping gaps. Then they can be pumped out via the pumping ports towards the TMPs or via the CVP, while others may return back to the plasma vessel through the leakage openings/gaps and the pumping gaps. In Figure 1, the different types of leakage gaps are shown (horizontal, vertical, toroidal, and poloidal). (For a more detailed visualization, see Ref. [12].) In this work, the leakages are divided into two main categories: one corresponding to the entire AEH section and the other to the AEP section. The present divertor geometry has been extracted from the corresponding detailed CATIA model and has been processed using the open-source SALOME suite [28]. The main assumption of the proposed simplified model is that the complex divertor geometry is broken down into reservoirs connected by cylindrical channels with known lengths (L) and diameters (D). Specifically, the geometry was represented using 2, 3, or 4 reservoirs. The number and position of reservoirs were chosen to correspond to physically distinct sub-divertor regions of W7-X, rather than being arbitrary numerical subdivisions. As a representative example, the configuration of the connected channels and reservoirs for the 3-reservoir model will be explained. Figure 2 serves as a guide to understand the model construction process for the 3-reservoir model, while in Figure 3 the three different model configurations are shown. Firstly, the three reservoirs were positioned at their respective locations within the divertor volume and are represented by the spheres R_1, R_2, and R_3 in Figure 2.

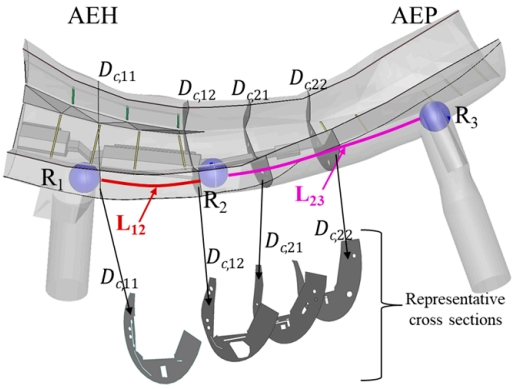

Figure 2. Representation of how the geometrical characteristics are derived for the 3-reservoir conductance model.

The reservoirs are connected in series by cylindrical channels, with one channel connecting R_1 and R_2 and another connecting R_2 and R_3. The channel lengths (L_{12} and L_{23}) correspond to the distances between the reservoirs, derived from the CATIA model. The diameter of the channels was determined with the help of cross-sections extracted at multiple locations throughout the divertor, as illustrated in Figure 2. More specifically, between the spheres, several cross-sections have been considered and from their surface the diameter was calculated. The surface area of each cross-section was obtained from the processing of the geometry files, and the circular diameter (D_c) was subsequently derived from these areas as

$$D_c = \sqrt{\frac{4 \times A}{\pi}}, \tag{1}$$

where A is the surface in m^2. The average diameter across all cross-sections between the two spheres is then calculated, and the resulting channel diameter for two channels is expressed as $D_{12} = \frac{D_{c,11}+D_{c,12}+\ldots+D_{c,1n}}{n}$ and $D_{23} = \frac{D_{c,21}+D_{c,22}+\ldots+D_{c,2n}}{n}$. Additional details regarding the geometric characteristics of the channels for each model are provided in Section 2.2.

2.2. Different Types of Examined Conductance Models: 2-, 3-, and 4-Reservoir Models

Several set-ups were studied in the present work. Specifically, in order to explore the balance between simplicity and accuracy, the following models are considered and shown in Figure 3: a 2-reservoir model, 3-reservoir model, and 4-reservoir model.

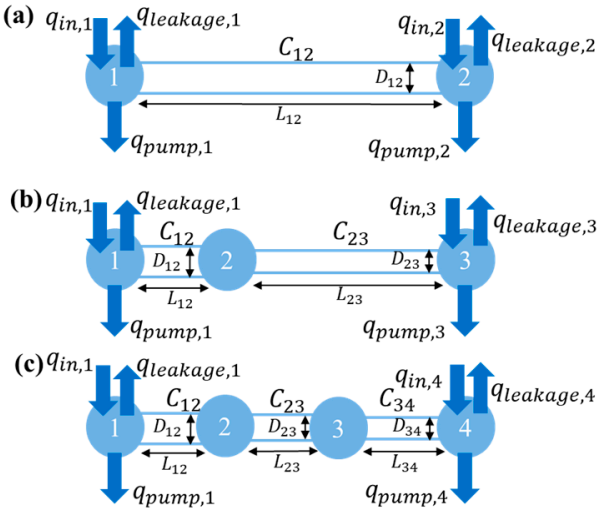

Figure 3. Visual representation of the 2-reservoir (**a**), 3-reservoir (**b**), and 4-reservoir (**c**) models.

Each reservoir has an input, a pumped-out throughput, and losses due to leakages. The simplest 2-reservoir model treats R_1 and R_3 from Figure 2 as the only two reservoirs, connected by a single channel, which has diameter $D_{12} = 0.61$ m and length $L_{12} = 4$ m (here, the diameter is determined as described in Section 2.1, while the length corresponds to the actual distance between the reservoirs). Table 1 summarizes the geometrical input parameters used in the conductance models. This configuration gives a basic estimate of the pressure at the AEH and AEP sections but tends to oversimplify the internal pressure distribution. The system of equations for this model, derived from the principle of mass conservation, which corresponds to Figure 3a is given as

$$\begin{aligned} q_{in,1} - q_{leakage,1} - C_{12} \times (p_1 - p_2) - q_{pump,1} = 0, \\ q_{in,2} - q_{leakage,2} + C_{12} \times (p_1 - p_2) - q_{pump,2} = 0, \end{aligned} \tag{2}$$

where q_{in} is the net incoming throughput (Pa m^3/s) for the AEH and AEP regions, $q_{leakage}$ is the throughput through the leakages that returns to the plasma region, q_{pump} is the throughput resulting from the pumping, C_{12} is the conductance (m^3/s) of the channel between the two reservoirs of Figure 3a, and p is the pressure (Pa). The net incoming throughput is derived from the total incoming neutral flux entering the divertor through the pumping gaps, minus the portion of the flux that returns to the plasma region via the same gaps (outflux). Based on the direction of the flow (to the right or to the left), the value of $C_{12} \times (p_1 - p_2)$ can be positive or negative.

Table 1. Geometrical input parameters used in the conductance model.

Model	Channel	Channel Diameter D (m)	Channel Length L (m)
2-reservoir	R_1-R_2	0.61	4.0
3-reservoir	R_1-R_2	0.625	1.7
3-reservoir	R_2-R_3	0.56	2.3
4-reservoir	R_1-R_2	0.625	1.7
4-reservoir	R_2-R_3	0.60	1.0
4-reservoir	R_3-R_4	0.56	1.3

To improve accuracy, a reservoir between the AEH and AEP sections is introduced, providing a more realistic pressure gradient across the sub-divertor. This is the 3-reservoir model shown both in Figures 2 and 3b. This configuration includes two channels as described in Section 2.1, with diameters $D_{12} = 0.625$ m and $D_{23} = 0.56$ m and lengths $L_{12} = 1.7$ m and $L_{23} = 2.3$ m. In this case, the system of equations becomes

$$\begin{aligned} q_{in,1} - q_{leakage,1} - C_{12} \times (p_1 - p_2) - q_{pump,1} = 0, \\ q_{in,3} - q_{leakage,3} + C_{23} \times (p_2 - p_3) - q_{pump,3} = 0, \\ C_{12} \times (p_1 - p_2) - C_{23} \times (p_2 - p_3) = 0, \end{aligned} \tag{3}$$

Finally, a model with four reservoirs is considered to achieve better pressure resolution between the AEH and AEP sections. In this configuration, an additional reservoir is added between the reservoirs R_2 and R_3 of Figure 2, while the remaining three reservoirs retain their original positions. In Figure 3c, a schematic representation of this model is shown. The diameter and length of the channel between the R_1 and R_2 reservoir is $D_{12} = 0.625$ m and $L_{12} = 1.7$ m, between the second and the additional third reservoir $D_{23} = 0.6$ m and

$L_{23} = 1$ m, and between the third and fourth reservoir $D_{34} = 0.56$ m and $L_{34} = 1.3$ m. The new system of equations is described as

$$\begin{aligned} q_{in,1} - q_{leakage,1} - C_{12} \times (p_1 - p_2) - q_{pump,1} &= 0, \\ q_{in,4} - q_{leakage,4} + C_{34} \times (p_3 - p_4) - q_{pump,4} &= 0, \\ C_{12} \times (p_1 - p_2) - C_{23} \times (p_2 - p_3) &= 0, \\ C_{23} \times (p_2 - p_3) - C_{34} \times (p_3 - p_4) &= 0. \end{aligned} \tag{4}$$

To close the system of equations, the expressions for the throughput and conductance must be specified. The relevant formulas are provided in Sections 2.3 and 2.4. The Newton–Raphson method is employed to numerically solve the system of equations for each model, yielding the pressure values and the leakage fluxes. The computational cost of this method is negligible, with solutions obtained within a few seconds on a standard laptop. This makes the approach well-suited for fast calculations, even with limited computational resources. This efficiency makes the conductance model particularly advantageous for parametric studies or sensitivity analyses, where numerous simulations are required. The model cannot fully replace comprehensive 3D simulations. However, it offers a practical alternative with acceptable uncertainty, capturing essential pressure distribution features at a much lower computational cost.

2.3. Throughput Formulas

Within the system of equations presented in Section 2.2, the throughputs corresponding to leakage, pumping, and net incoming flux must be defined. These throughput terms provide the necessary closure for the system, along with the conductance formula, enabling the calculation of pressure and neutral flux values. For the definition of the throughput at the leakages, the following approximation is used [10]:

$$q_{leakage} = \mathrm{B} \times \frac{1}{4} \times A_{leakage} \times p \times \sqrt{\frac{8 \times k_B \times T_{leakage}}{\pi \times m}}, \tag{5}$$

where

$$\mathrm{B} = \exp\left[-s^2 \times \cos\theta^2\right] + \sqrt{\pi} \times s \times \cos\theta \times [1 + \mathrm{erf}(s \times \cos\theta)], \tag{6}$$

where k_B is the Boltzmann constant, m is the molar mass of hydrogen (3.34×10^{-27} kg for H_2), and $A_{leakage}$ is the surface of the leakages. The $A_{leakage}$ for the AEH section is 7.7×10^{-2} m^2 and for the AEP section it is 5.52×10^{-2} m^2. Also, $T_{leakage}$ is the temperature around the leakage gaps. Specifically, the temperature employed in the calculations corresponds to the temperature of the vessel, and it is equal to 303 K (from Ref. [12]). The throughput was calculated by assuming a Maxwellian distribution [10]. Specifically, the fluxes were modeled using a shifted Maxwellian distribution (a Maxwellian distribution with an imposed bulk flow velocity) B, as this approach is generally expected to yield more accurate results. The shift parameter s in Equation (6) was applied based on D.C. Wadsworth's theory [29] applying the free molecular assumption: $s = 0.5/\sqrt{\pi}$. The angle θ defines the orientation of the velocity relative to the major axis of the orbit. In this work, it is assumed to be equal to 0°.

The pumping throughput includes the pumped particle flux at the pumping ports going to the turbomolecular pumps and the pumping through the cryopump. In the cases studied, summarized in Table 2, different pump configurations are considered: with either both types of pumps or only one active.

Table 2. The cases studied for the conductance model.

Cases	AEH Flux	AEP Flux	CVP Status	TMP Status
1	1×10^{20}	1×10^{21}	ON	ON
2	1×10^{21}	1×10^{20}	ON	ON
3	1×10^{22}	1×10^{21}	ON	ON
4	1×10^{21}	1×10^{22}	ON	ON
5	1×10^{20}	1×10^{21}	OFF	ON
6	1×10^{21}	1×10^{20}	OFF	ON
7	1×10^{22}	1×10^{21}	OFF	ON
8	1×10^{21}	1×10^{22}	OFF	ON
9	1×10^{20}	1×10^{21}	ON	OFF
10	1×10^{21}	1×10^{20}	ON	OFF
11	1×10^{22}	1×10^{21}	ON	OFF
12	1×10^{21}	1×10^{22}	ON	OFF
13	1×10^{20}	1×10^{20}	ON	ON
14	1×10^{21}	1×10^{21}	ON	ON
15	1×10^{22}	1×10^{22}	ON	ON
16	1×10^{22}	1×10^{23}	ON	ON
17	1×10^{23}	1×10^{22}	ON	ON

For the turbomolecular pumps, the throughput is defined as

$$q_{TMP} = s_{eff} \times p, \tag{7}$$

$$s_{eff} = \frac{1}{4} \times \xi_{TMP} \times A_{port} \times \sqrt{\frac{8 \times k_B \times T_{vessel}}{\pi \times m}}, \tag{8}$$

where s_{eff} is the pumping speed at the ports, T_{vessel} is the temperature of the vessel (303 K), and ξ_{TMP} is the capture coefficient. The capture coefficient ξ_{TMP} represents the probability of a particle being pumped and serves as a measure of the vacuum pump efficiency. In all simulations presented here, it is an input parameter as in Ref. [12]. The ξ_{TMP} for the AEH port is 0.06 and for the AEP port it is 0.0264. The surface of the pumping port A_{port} is the same for the AEH and AEP section (see Figure 1), and it is equal to 0.124 m^2.

For the cases in which the cryopump is considered, the throughput through the cryopump, q_{cp}, is calculated as

$$q_{cp} = \left\{ \frac{1}{4} \times \left[\left(\xi_{cp,small} \times A_{cp,small} \right) + \left(\xi_{cp,big} \times A_{cp,big} \right) \right] \sqrt{\frac{8 \times k_B \times T_{cp}}{\pi \times m}} \right\} p, \tag{9}$$

where $A_{cp,small} = 0.09$ m^2, $A_{cp,big} = 0.18$ m^2, $\xi_{cp,small} = 0.092/0.12$, and $\xi_{cpbig} = 0.096/0.12$ [12], for the small and large modules of the cryopump for incoming flux of 10^{20}–10^{21}, 10^{21}–10^{22}/10^{22}–10^{23}, respectively, and T_{cp} is the temperature at the entrance of the cryopump (300 K as in Ref. [12]).

The net incoming throughput for the AEH and AEP sections is evaluated using three approaches (scenarios A, B, and C). The purpose of this comparison is to evaluate the extent to which the model can be formulated independently of adjustable input parameters, as well as to quantify the deviations that arise at varying levels of such independence. The scenarios differ in the method used to estimate the net incoming throughput, which is defined as the total neutral flux entering the divertor through the pumping gaps minus the flux that returns to the plasma region through the same gaps (outflux). The incoming flux through the AEP and AEH sections is shown in Table 2. Scenario A corresponds to

the calculation of the net incoming throughput which exactly matches the net throughput values predicted by DIVGAS, as in

$$q_{in} = F_{in} \times T_0 \times k_B - F_{out} \times T_0 \times k_B, \quad (10)$$

where F_{in} (H_2 s^{-1}) is the incoming flux (shown in Table 1 for all of the different cases studied for the AEH and AEP sections), T_0 is the temperature at the inlet AEH and AEP areas (600 K as in [12]), and F_{out} (H_2 s^{-1}) is the outflux that returns to the plasma region through the AEH and AEP pumping gaps. It is noted that in the DIVGAS simulations, the incoming flux is provided as an input parameter, while the outflux is obtained as part of the DIVGAS solution. In scenario A, the exact DIVGAS outflux is used in the conductance model. Thus, scenario A is mainly incorporated in this study and is used as a baseline for comparison with the other two scenarios. In all cases, it was observed that the net incoming flux at the AEH section became negative whenever the incoming flux at the AEP section exceeded that at the AEH section. This observation was considered as the baseline assumption for scenario B. In scenario B, the cases were divided into two groups based on the incoming flux: one group with cases where the net incoming flux through the AEP section is higher than the incoming flux through the AEH section and one group with the other cases studied. For each of the two groups, using the DIVGAS results [12], the ratio of outflux to incoming flux was calculated separately for the AEH and AEP sections. The average values of these ratios, computed over the different cases studied, were used as representative values in place of the individual outfluxes. Specifically, for the cases with higher incoming flux at the AEP section, the final ratios were 1.92 and 0.317 for the AEH and AEP sections, respectively. For the other cases, the corresponding values were 0.729 and 0.595 for the AEH and AEP sections, respectively. It is evident that scenario B does not require the exact outflux for each case; instead, the outflux in the conductance model is obtained using calibrated values derived from DIVGAS. Scenario C does not use the outflux values from DIVGAS, making the model fully independent. In this scenario, the free molecular flow assumption is applied, as in the throughput through the leakage gaps in Equation (5), with the temperature at the inlet, T_0, and the surface of the AEH and AEP pumping gaps ($A_{AEH} = 0.153$ m^2 and $A_{AEP} = 0.0450$ m^2).

2.4. Conductance Formula

To connect the reservoirs in the different types of conductance models (2-, 3-, and 4-reservoirs), the formula that connects each channel needs to be defined. The conductance of the channels depends on the geometry of the connecting channels (length, diameter, and cross-section) and the flow regime, which is typically characterized by the Knudsen number (Kn). The Kn number, which is defined as the ratio of the mean free path over a representative characteristic length, is calculated using the hard-sphere gas model as

$$Kn = \frac{1}{\sqrt{2} \times \pi \times n \times d^2 \times l}, \quad (11)$$

where n is the density (kg/m^3), d the diameter for hydrogen (which is taken from Ref. [12] for comparative purposes equal to 2.92×10^{-10} m), and l the characteristic length (m). In this work, l is the diameter at the AEH and AEP cross-sections of the sub-divertor area. Table 2 summarizes all the cases investigated in this work, covering a wide range of flow regimes. The cases are characterized by Knudsen numbers between 0.005 and 14, which cover the whole range of rarefaction from continuum to free molecular regime. For the problem under investigation, the Knudsen numbers correspond to neutral pressures ranging from approximately 0.002 to 7.9 Pa.

In general, in the sub-divertor region of W7-X, the gas flow often falls within the transitional regime, between free molecular flow and viscous laminar flow. Therefore, a conductance formula also applicable to this regime is required. It is important to note that various empirical and analytical formulas exist in the literature for estimating gas conductance under different conditions [22,30,31]. Considering the specific geometry of the sub-divertor and the transitional nature of the flow, the formulation presented in Ref. [31] was selected and adapted to the conductance model of this work for its applicability and its ability to provide a good balance between simplicity and accuracy within the relevant parameter space. The conductance formula applied in the model is defined as follows [31]:

$$C = \frac{q_{MK}}{(p_u - p_d)}, \quad \text{with}$$
$$q_{MK} = \frac{q_{VL} \times q_{TB} \times \left(q_{CF} - \frac{q_M}{1.235}\right)}{\sqrt{{q_{VL}}^2 \times {q_{TB}}^2 + {q_{TB}}^2 \times \left(q_{CF} - \frac{q_M}{1.235}\right)^2 + \left(q_{CF} - \frac{q_M}{1.235}\right)^2 \times {q_{VL}}^2}} + q_M \times \frac{1 + \sqrt{\frac{m}{k_B \times T_{vessel}}} \times \frac{\widetilde{p}}{\mu}}{1 + 1.235 \times \sqrt{\frac{m}{k_B \times T_{vessel}}} \times \frac{\widetilde{p}}{\mu}} \quad (12)$$

where p_u and p_d are the upstream and downstream pressures for a specific channel, q_{MK} is the throughput (Pa m^3/s) obtained by the Modified Knudsen equation [31], $\widetilde{p}$ is the mean pressure between the channel ends, and μ is the viscosity of the working gas. Equation (12) is incorporated into the algebraic systems (2), (3), and (4) corresponding to the models with two, three, and four reservoirs, respectively, in order to describe the conductance channels between the reservoirs. The quantities q_{VL}, q_{TB}, q_{CF}, q_M are the throughputs when calculated assuming viscous laminar flow, turbulent flow, compressible flow, and molecular flow, respectively, and are defined as in Ref. [31]. To enable a direct comparison between the results of the conductance model and the corresponding results from DIV-GAS, the viscosity of hydrogen was calculated using the hard-sphere model, assuming a molecular diameter of 2.92×10^{-10} m. The approximate Formula (12) blends the viscous and molecular contributions to conductance and is valid over a wide range of Knudsen numbers, particularly useful in transitional flow.

To evaluate the accuracy of the approximate conductance formula used in this study, it was benchmarked against DSMC data available in the literature [32], focusing on the transitional flow regime. Following Ref. [32], the benchmark problem that was considered is a simple case of gas flow through a straight channel with a circular cross-section. The comparison is shown in Figure 4, for a length-to-radius ratio L/R = 2, 5, and 10 and for different values of the local rarefaction parameter δ ($\delta \approx 1/Kn$), showing that the analytical approximation aligns closely with DSMC-based results.

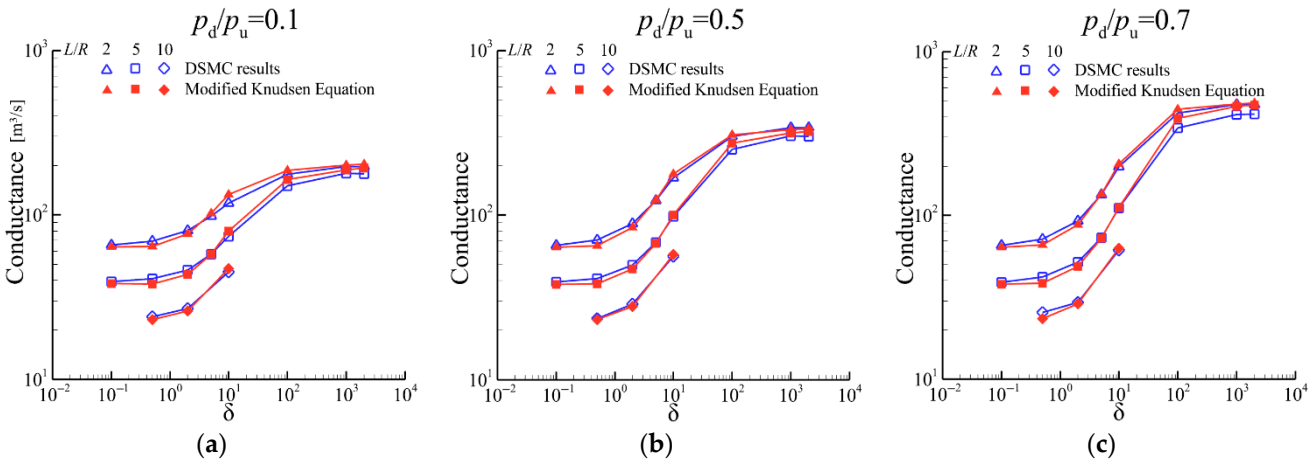

Figure 4. Conductance comparison between DSMC results [32] and the Modified Knudsen equation for (**a**) p_d/p_u = 0.1, (**b**) p_d/p_u = 0.5, and (**c**) p_d/p_u= 0.7.

In general, small deviations were observed (Figure 4). For the W7-X geometry, where the typical L/R is around 3–13 based on the different implemented conductance models (with 2-, 3-, and 4-reservoirs) and δ values vary between 0.1 and 200, the agreement between the approximate formula and DSMC results is good with maximum deviations of 14%. Given the good performance of the simplified conductance formula (Equation (12)), its use to describe the conductance of each channel in the simplified conductance models (see Section 2.2) is well justified.

3. Results and Discussion

To evaluate the performance of the simplified conductance model, it was tested across a series of 17 cases, as shown in Table 2, representative of actual operating conditions in the W7-X sub-divertor. These included varying incoming neutral fluxes at the AEH and AEP sections and different pumping configurations (TMP and CVP modules switched on/off). The results were compared to detailed 3D DIVGAS simulations [12]. Although scenario A (see Section 2.3) served as the baseline for studying the conductance model, the model was evaluated across all three scenarios from Section 2.3, namely A, B, and C.

Firstly, a comparison between the two-, three-, and four-reservoir configurations was carried out, shown in Figure 5, for scenario A. For each one of the three configurations, the deviation between the DIVGAS pressure results and the conductance model was calculated. The deviation is calculated as $Deviation(\%) = 100 \times (|p_{DIVGAS} - p_{Cond.Model}|)/p_{DIVGAS}$. In Figure 5, only the results for the AEH section are shown because similar trends among the three models were observed for the AEP section. As shown, the overall trend indicates that the three- and four-reservoir models yield a smaller average deviation compared to the two-reservoir model. The additional resolution introduced by the third reservoir allows for a more accurate representation of the pressure distribution across the sub-divertor area with an average deviation of 43%, whereas the model with two reservoirs shows an average deviation of 47%. It is also noteworthy that, while the maximum deviation among the 17 cases for the three-reservoir model is 93%, it increases to 113% for the two-reservoir model. While the four-reservoir model offers more geometrical accuracy, the difference between three and four reservoirs is generally minimal (less than 5%). Nevertheless, the four-reservoir model remains useful in cases where pressure values at an additional point are required.

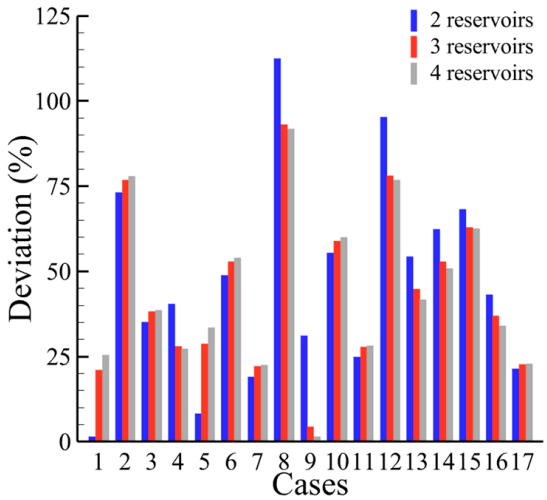

Figure 5. Comparison of pressure deviation between DIVGAS results and simplified conductance models with 2, 3, and 4 reservoirs under scenario A.

The comparison of the pressures between the conductance model with three reservoirs and DIVGAS simulations, using scenario A, is shown for the three main reservoirs in Figure 6: the AEH section (R1), the region between AEH and AEP (R2), and the AEP section (R3). The deviation in pressure prediction across all 17 test cases is presented for each reservoir, with corresponding error bars. These error bars account for the spatial variation in pressure observed within each reservoir area, based on spherical regions extracted from the DIVGAS simulations at the locations of the reservoirs (as shown in Figure 2). The pressure is not perfectly uniform inside these spherical zones, and the error bars reflect this variation and provide a more realistic image of the expected uncertainty.

The average deviation between the conductance model and DIVGAS is also shown in Figure 6 with a dashed line for each reservoir: 43% in the AEH section, 31% between the AEH and AEP areas, and 15% in the AEP section. Although not negligible, the observed deviations are deemed acceptable. This is especially true given the simplified conductance model and the highly complex three-dimensional sub-divertor geometry. The maximum deviation noticed is 93%, 78%, and 57% for the R1, R2, and R3 reservoirs, respectively, whereas the minimum deviation is around 4% among the three positions. The averaged deviation among all reservoirs is 32%. The overall agreement demonstrates that the conductance-based approach provides reasonable and reliable estimates for neutral gas pressure in the sub-divertor, even in the presence of localized pressure variations, with the majority of the cases to overestimate the DIVGAS results. Due to the simplified nature of the model, deviations cannot be uniquely attributed to individual physical mechanisms on a case-by-case basis, but instead reflect the cumulative impact of spatial averaging and geometric simplification.

Figure 7 also presents the deviations between DIVGAS and the conductance model at the additional location of the four-reservoir model, explained in Section 2.2. It also shows good agreement within an average error of 25%.

In addition, we tried to demonstrate the equivalence between the three-reservoir and two-reservoir models, using scenario A as a base. For this purpose, the equivalent conductance for the two channels in the three-reservoir model was calculated. Since the channels are connected in series, the equivalent conductance was obtained using the relation $C_{eq} = C_{12} * C_{23}/(C_{12} + C_{23})$, where C_{12} and C_{23} are the conductance values of the channels connecting the reservoirs R_1-R_2 and R_2-R_3, respectively, as shown in Figures 2 and 3. The equivalent conductance and the pressures from the three-reservoir model were then inserted into Equation (12), together with the channel length of the two-reservoir model (see Section 2.2), to determine an equivalent diameter. This procedure was repeated for all 17 cases considered, resulting in 17 equivalent diameters for the two-reservoir model. The average of these values, 0.56 m, was adopted as the representative equivalent diameter in the two-reservoir model. In Figure 8, a comparison between the deviations of the three-reservoir model and the two-reservoir model with the equivalent diameter is presented, relative to the DIVGAS results for the AEH section (a similar comparison was obtained for the AEP section). The application of the equivalent diameter substantially improved the performance of the two-reservoir model: the maximum deviation with respect to DIVGAS decreases from 113% (original two-reservoir model) to 88%, while the maximum deviation between the two-reservoir model with equivalent diameter and the three-reservoir models is mostly under 10%. The equivalent-diameter approach enables the simpler two-reservoir model to reproduce results that are much closer to those of the more detailed three-reservoir configuration at the same positions.

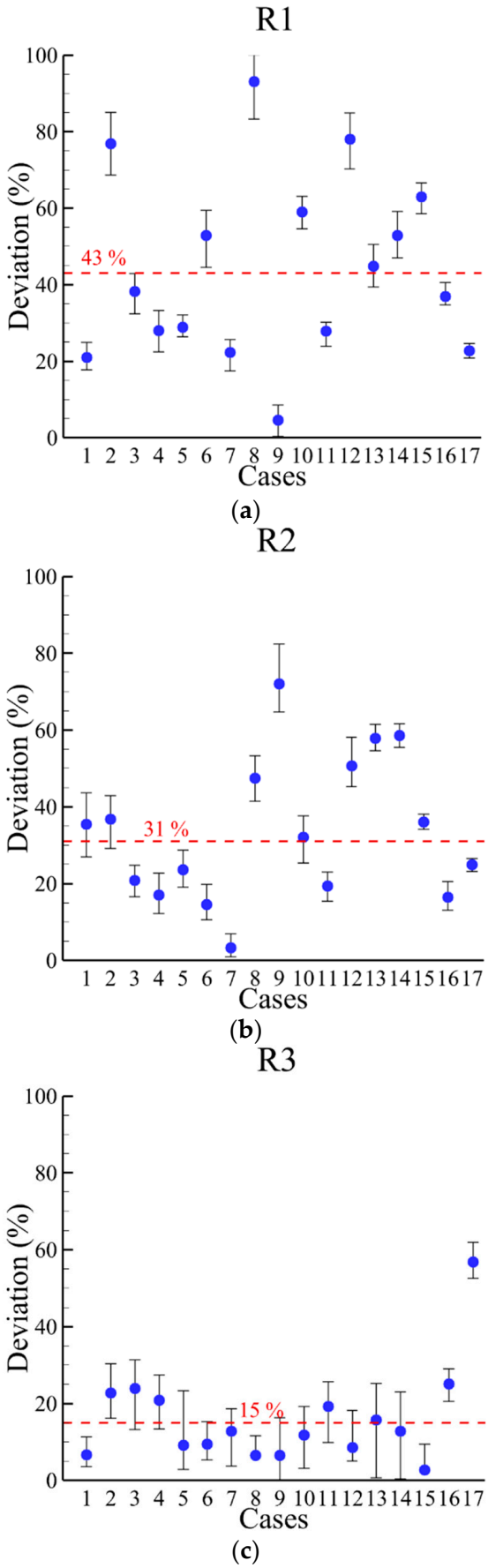

Figure 6. Pressure deviations between DIVGAS simulations and the conductance model at the three reservoirs: (**a**) R1 (AEH section), (**b**) R2 (between AEH and AEP), and (**c**) R3 (AEP section), for scenario A.

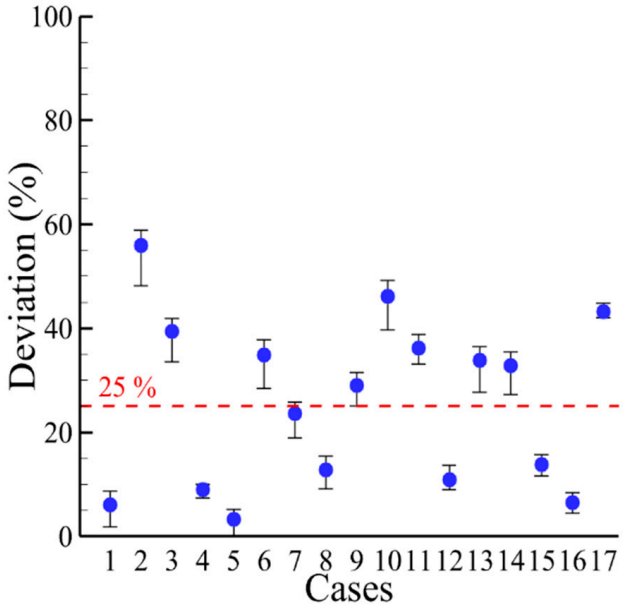

Figure 7. The pressure deviations between DIVGAS and the conductance model for the additional location at the 4-reservoir model.

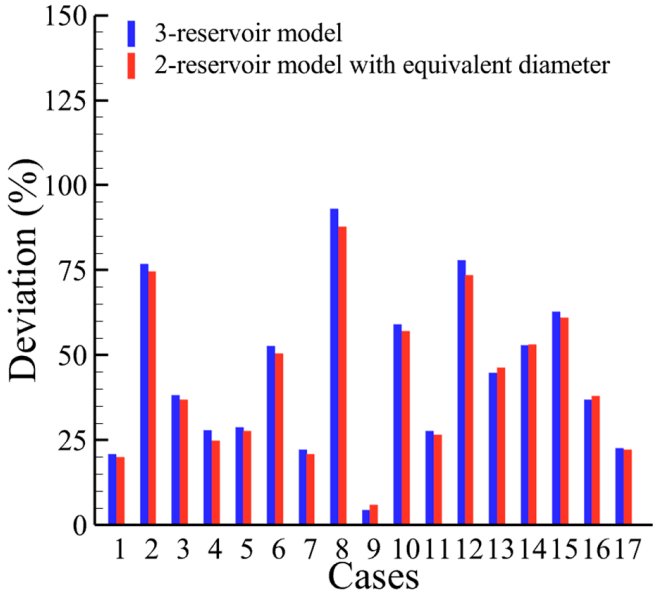

Figure 8. Comparison of the deviations with the DIVGAS results for the 3-reservoir model and the 2-reservoir model with the equivalent diameter.

In addition to scenario A, in Figure 9, the corresponding pressure deviations for scenarios B and C (as explained in Section 2.3) are presented. This study provides a useful reference for assessing the consistency and sensitivity of the results. Scenario B shows an average deviation with DIVGAS of 43%, 32%, and 18% at R1, R2, and R3, respectively. Scenario C shows an average deviation with DIVGAS of 52%, 34%, and 15% at R1, R2, and R3, respectively. Notably, even in the case that the outflux is calculated based on Equation (5), the deviation from the DIVGAS-based results remains relatively near, suggesting that the simplified model still captures the essential behavior of the system. The deviations remain relatively small even as the model becomes more independent (scenarios B and C), indicating that the simplified conductance model retains good predictive capability without heavy reliance on detailed simulation data.

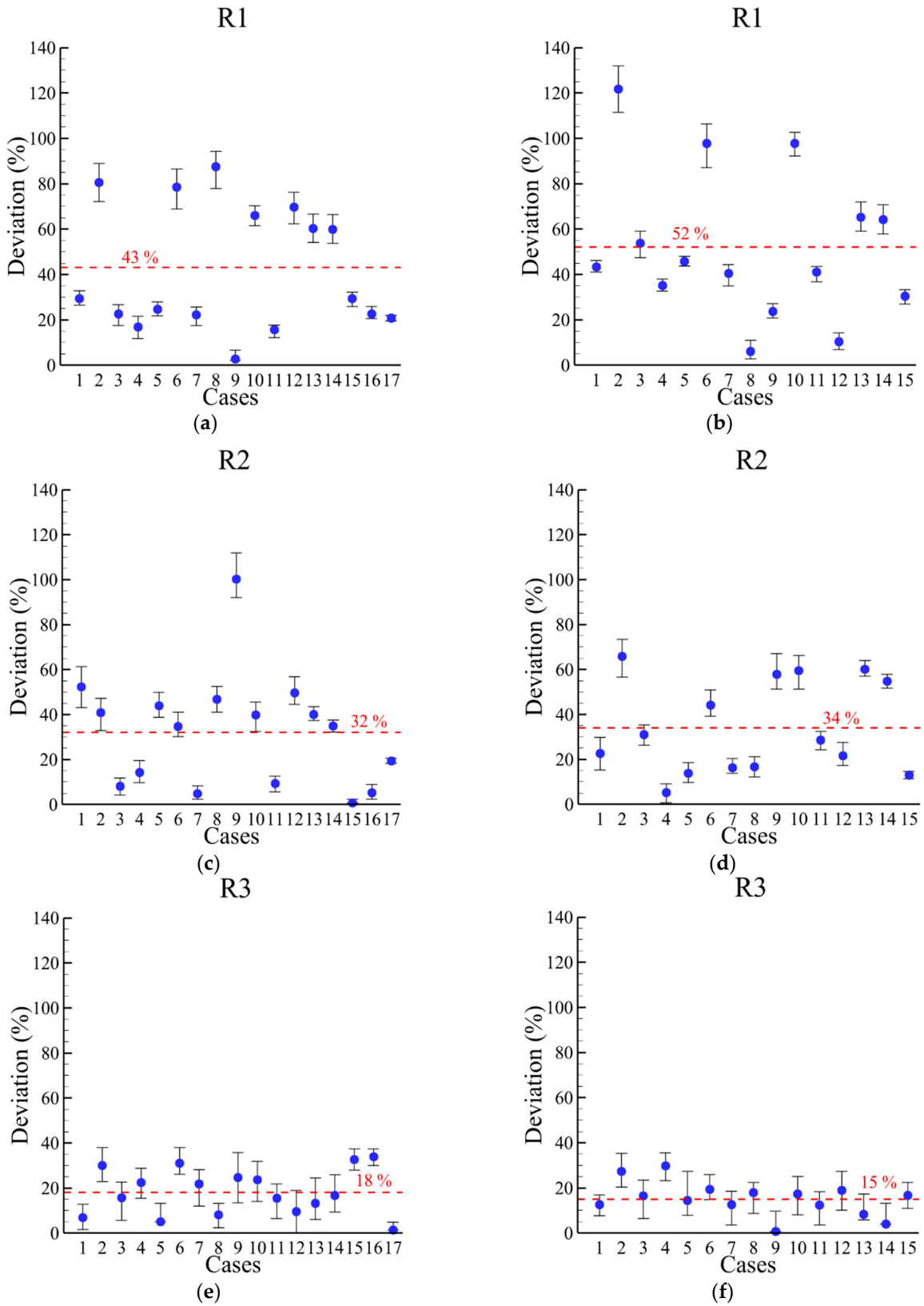

Figure 9. The pressure deviations between DIVGAS and the conductance model at the three reservoirs R1 (**a**,**b**), R2 (**c**,**d**), and R3 (**e**,**f**), for scenarios B (**a**,**c**,**e**) and C (**b**,**d**,**f**).

To improve the agreement between the conductance model pressures and the corresponding DIVGAS pressures, individual scaling factors were determined for each of the 17 cases. For a given case *i* (from the 17 cases), the optimal scaling factor (*k*) was computed

as the ratio between the DIVGAS value and the conductance model value from scenario B. The scaling factors at the three positions R1, R2, and R3 are defined as

$$k_{1,i} = \frac{p_{DIVGAS,1,i}}{p_{Cond.Model,1,i}}, \quad k_{2,i} = \frac{p_{DIVGAS,2,i}}{p_{Cond.Model,2,i}}, \quad k_{3,i} = \frac{p_{DIVGAS,3,i}}{p_{Cond.Model,3,i}}, \tag{13}$$

Next, an overall average scaling factor was obtained by averaging all of the individual scaling factors across the corresponding cases. Thus, an average k value was obtained: $k = 0.884$. The conductance model is subsequently calibrated by using the normalized pressures, p/k, instead of the absolute p. After implementing this normalization, the overall average deviation across the 3 positions and the 17 cases was 23%. More specifically, the average deviation with DIVGAS is 30%, 22%, and 17% at R1, R2, and R3, respectively.

The validation of the conductance model (scenario B) with the scaling factors is further extended in Figure 10. In Ref. [12], DIVGAS simulations were coupled with EMC3-EIRENE plasma simulations, in which DIVGAS receives the distribution of the incoming neutral fluxes at AEP (small) and AEH (large) pumping gaps as input from the plasma simulations. In addition, in Ref. [12], correlations between the sub-divertor pressure and the incoming flux at the AEH and AEP sections were proposed (fitting correlations). In Figure 10, a comparison between the correlations, the coupled DIVGAS+EMC3-EIRENE results from Ref. [12], and the calibrated conductance model is shown. As seen, good agreement is observed between the conductance model, the DIVGAS simulations coupled with EMC3-EIRENE plasma data, and the fitting correlations from Ref. [12]. The DIVGAS simulations coupled to EMC3-EIRENE plasma calculations correspond to operating points different from the 17 benchmark cases considered in this study. Therefore, Figure 10 serves as an additional validation of the conductance model beyond the benchmarked scenarios.

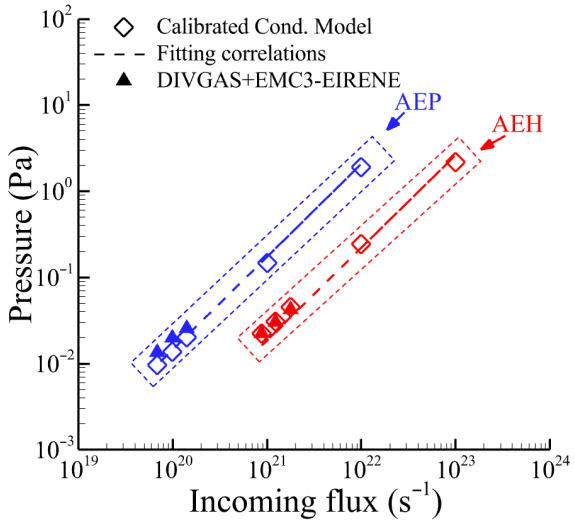

Figure 10. Neutral gas pressures at the AEH and AEP sections as a function of the incoming neutral flux at the respective openings, as predicted by the calibrated conductance model, compared with DIVGAS–EMC3-EIRENE results and fitting correlations from Ref. [12].

In addition to the pressure comparison, the deviation in leakage fluxes between the conductance model and DIVGAS simulations was analyzed to further evaluate the performance of the simplified approach in terms of leakage fluxes. In Figure 11, the deviations of the fluxes are shown for both the AEH and AEP sections using scenario A. The results show that the prediction of leakage fluxes is generally more challenging than pressure estimation, leading to larger deviations. This may be attributed to the strong sensitivity of the leakage flux to local geometric details, surface areas, and temperature variations at the leakage loca-

tions, factors that are difficult to fully capture in a simplified, reduced-order conductance model. Across all analyzed cases, the average leakage flux deviation near the AEH section was approximately 94%, which is considered acceptable given the complexity of the system and the level of simplification applied. However, the error increases significantly near the AEP section, reaching an average of around 160%. The large deviations observed in the leakage flux predictions highlight the limitations of the simplified conductance model, particularly for quantities such as pressure that are highly sensitive to local geometrical effects. Leakage fluxes depend strongly on many parameters such as three-dimensional effects, temperature variations, etc., all of which are fully captured in the DIVGAS simulations but are only approximated or averaged in the simplified model. To improve predictive accuracy, future work could focus on implementing complex network channel representations with increased geometric fidelity, incorporating advanced optimization and artificial-intelligence-driven calibration strategies, or developing hybrid multi-fidelity approaches that combine the conductance model with high-fidelity simulations. These strategies are expected to enhance pressure and flux predictions while retaining computational efficiency. Despite these challenges, it is important to emphasize that the conductance model still captures the general trend and order of magnitude of the leakage fluxes, providing useful insights for engineering design and parametric studies. Nevertheless, these findings highlight that while the simplified conductance model offers good predictive capability for pressure distributions, greater caution is required when interpreting leakage flux results. Notably, applying scenario B with the scaling factors reduces the deviations to 69% and 120% for the AEH and AEP sections, respectively, demonstrating an improvement in model accuracy.

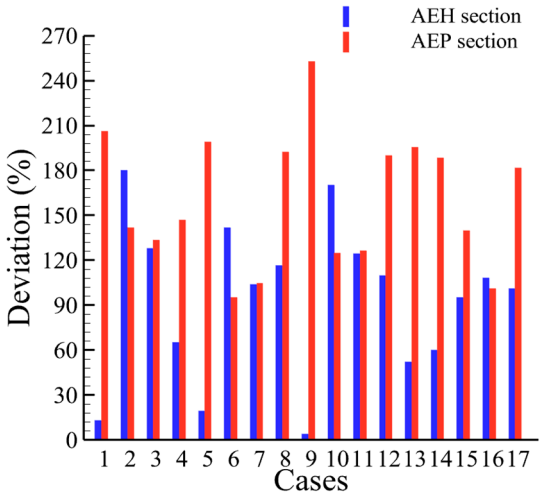

Figure 11. Comparison of leakage fluxes derived from DIVGAS simulations and the conductance model at the AEH and AEP sections for scenario A.

An additional analysis was conducted to evaluate the effect of the shifted Maxwellian distribution B from Equation (6) on the pressures and fluxes. Since the optimal case is scenario B with the scaling factors, it was used to recalculate all the values with the non-shifted Maxwellian. The results indicate that the average pressure deviations increase to 88%, 67%, and 40% at R1, R2, and R3, respectively. Conversely, the flux deviations decrease to 62% and 101% for the AEH and AEP sections, respectively.

4. Conclusions

In this study, a simplified conductance-based model was developed and applied to estimate neutral gas pressures and leakage fluxes in the sub-divertor region of the

W7-X stellarator. In the model, the complex sub-divertor area is replaced by virtual reservoirs which are connected by straight pipes, with the conductance for each channel being approximated by a formula valid across a wide range of Knudsen numbers. The conductance model was tested across 17 different operating scenarios, varying neutral fluxes and pumping configurations, and the results were compared to DIVGAS simulations.

In conclusion, the simplified conductance model developed and benchmarked here offers a practical tool for estimating pressure distributions and neutral particle fluxes, two important quantities that play a vital role in assessing pumping efficiency in the W7-X divertor. In the best case (scenario B with scaling factors), the simplified model predicted pressures with a mean deviation of 23% relative to the DIVGAS results. Nonetheless, greater deviations are shown in flux predictions. The higher deviation may be attributed to the simplified geometry considerations in the model. This level of agreement can be considered reasonable for engineering applications and preliminary design studies. This conductance model is particularly suitable for parametric scans where rapid feedback is required, given the low computational cost of the model. Several different model types were studied, however, for a more independent approach; scenario B with the scaling factors applied is recommended for future studies. Future work includes applying this simplified model to other fusion devices with more complex divertor geometries, as well as continuing the development of a more advanced network code. The proposed conductance models could be integrated to codes such as EMC3-EIRENE and support the optimization of W7-X and future fusion machines' pumping system performance.

Author Contributions: Conceptualization, C.T., F.L., V.H. (Volker Hauer), V.H. (Victoria Haak), D.N., and C.-P.D.; methodology, C.T., F.L., V.H. (Volker Hauer), V.H. (Victoria Haak), D.N., and C.-P.D.; software, F.L. and C.T.; validation, F.L. and C.T.; formal analysis, F.L. and C.T.; investigation, C.T., F.L., V.H. (Volker Hauer), V.H. (Victoria Haak), D.N., and C.-P.D.; resources, F.L., C.T., and W7-X Team; data curation, F.L. and C.T.; writing—original draft preparation, F.L., C.T., V.H. (Volker Hauer), V.H. (Victoria Haak), D.N., and C.-P.D.; writing—review and editing, F.L., C.T., V.H. (Volker Hauer), V.H. (Victoria Haak), D.N., and C.-P.D.; visualization, F.L. and C.T.; supervision, C.T.; project administration, C.T. and D.N.; funding acquisition, C.T. and D.N. All authors have read and agreed to the published version of the manuscript.

Funding: This research received no external funding.

Data Availability Statement: The data that supports the findings of this study are available within this article. Additional data may be made available upon reasonable request from the corresponding author.

Acknowledgments: This work has been carried out within the framework of the EUROfusion Consortium, funded by the European Union via the Euratom Research and Training Programme (Grant Agreement No 101052200—EUROfusion). The views and opinions expressed are, however, those of the author(s) only and do not necessarily reflect those of the European Union or the European Commission. Neither the European Union nor the European Commission can be held responsible for them. Moreover, we acknowledge support by the KIT Publication Fund of the Karlsruhe Institute of Technology. See Grulke et al. 2024, https://doi.org/10.1088/1741-4326/ad2f4d (accessed on 10 January 2026), for the W7-X Team.

Conflicts of Interest: The authors declare no conflicts of interest.

References

1. Federici, G.; Bachmann, C.; Barucca, L.; Baylard, C.; Biel, W.; Boccaccini, L.V.; Bustreo, C.; Ciattaglia, S.; Cismondi, F.; Corato, V.; et al. Overview of the DEMO staged design approach in Europe. *Nucl. Fusion* **2019**, *59*, 066013. [CrossRef]
2. Creely, A.J.; Greenwald, M.J.; Ballinger, S.B.; Brunner, D.; Canik, J.; Doody, J.; Fülöp, T.; Garnier, D.T.; Granetz, R.; Gray, T.K.; et al. Overview of the SPARC tokamak. *J. Plasma Phys.* **2020**, *86*, 865860502. [CrossRef]

3. Song, Y.; Li, J.; Wan, Y.; Liu, Y.; Wang, X.; Wan, B.; Fu, P.; Weng, P.; Wu, S.; Duan, X.; et al. Engineering design of the CFETR machine. *Fusion Eng. Des.* **2022**, *183*, 113247. [CrossRef]
4. ITER—The Way to New Energy. Available online: https://www.iter.org/ (accessed on 20 August 2025).
5. Hirsch, M.; Baldzuhn, J.; Beidler, C.; Brakel, R.; Burhenn, R.; Dinklage, A.; Ehmler, H.; Endler, M.; Erckmann, V.; Feng, Y.; et al. Major results from the stellarator Wendelstein 7-AS. *Plasma Phys. Control. Fusion* **2008**, *50*, 053001. [CrossRef]
6. Motojima, G.; Masuzaki, S.; Morisaki, T.; Tanaka, H.; Sakamoto, R.; Murase, T.; Oliver, S.; Kobayashi, M.; Shoji, M.; Tokitani, M.; et al. New approach to the control of particle recycling using divertor pumping in the Large Helical Device. *Nucl. Fusion* **2019**, *59*, 086022. [CrossRef]
7. Lion, J.; Anglès, J.C.; Bonauer, L.; Bañón Navarro, A.; Cadena Ceron, S.A.; Davies, R.; Drevlak, M.; Foppiani, N.; Geiger, J.; Goodman, A.; et al. Stellaris: A high-field quasi-isodynamic stellarator for a prototypical fusion power plant. *Fusion Eng. Des.* **2025**, *214*, 114868. [CrossRef]
8. Beidler, C.; Grieger, G.; Herrnegger, F.; Harmeyer, E.; Kisslinger, J.; Lotz, W.; Maassberg, H.; Merkel, P.; Nührenberg, J.; Rau, F.; et al. Physics and engineering design for Wendelstein VII-X. *Fusion Technol.* **1990**, *17*, 148–168. [CrossRef]
9. Klinger, T.; Baylard, C.; Beidler, C.D.; Boscary, J.; Bosch, H.S.; Dinklage, A.; Hartmann, D.; Helander, P.; Maßberg, H.; Peacock, A.; et al. Towards assembly completion and preparation of experimental campaigns of Wendelstein 7-X in the perspective of a path to a stellarator fusion power plant. *Fusion Eng. Des.* **2012**, *88*, 461–465. [CrossRef]
10. Bird, G.A. *Molecular Gas Dynamics and the Direct Simulation of Gas Flows*; Oxford Engineering Science Series; Clarendon Press (Oxford University Press): Oxford, NY, USA, 1994; ISBN 978-0-19-856195-8.
11. Sharipov, F. *Rarefied Gas Dynamics: Fundamentals for Research and Practice*; Wiley-VCH Verlag GmbH & Co. KGaA: Weinheim, Germany, 2016; ISBN 978-3-527-68553-0.
12. Varoutis, S.; Tantos, C.; Strobel, H.; Boeyaert, D.; Igitkhanov, Y.; Litovoli, F.; Dhard, C.P.; Haak, V.; Naujoks, D.; W7-X Team. Numerical analysis of gas exhaust in Wendelstein 7-X using the direct simulation Monte Carlo method. *Nucl. Fusion* **2025**, *65*, 076001. [CrossRef]
13. Tantos, C.; Varoutis, S.; Hauer, V.; Day, C.; Innocente, P. 3D numerical study of neutral gas dynamics in the DTT particle exhaust using the DSMC method. *Nucl. Fusion* **2024**, *64*, 016019. [CrossRef]
14. Tantos, C.; Strobel, H.; Hauer, V.; Day, C.; Giegerich, T.; Innocente, P. Numerical investigation of the DTT cryopump performance via 3D Direct Simulation Monte Carlo modeling. *Fusion Eng. Des.* **2025**, *215*, 115021. [CrossRef]
15. Varoutis, S.; Igitkhanov, Y.; Day, C.; Strobel, H.; Wenninger, R. Effect of neutral leaks on pumping efficiency in 3D DEMO divertor configuration. *Fusion Eng. Des.* **2018**, *136*, 1135–1139. [CrossRef]
16. Tantos, C.; Varoutis, S.; Day, C. Deterministic and stochastic modeling of rarefied gas flows in fusion particle exhaust systems. *J. Vac. Sci. Technol. B* **2020**, *38*, 064201. [CrossRef]
17. Gleason González, C. Modelling and Validation of Neutral Particle Flow by Means of Stochastic Algorithms Using the Example of a Fusion Divertor. Ph.D. Thesis, Karlsruhe Institute of Technology, Karlsruhe, Germany, 2022. [CrossRef]
18. Varoutis, S.; Tantos, C.; Strobel, H.; Day, C.; Dhard, C.P.; Haak, V.; Igitkhanov, Y.; Naujoks, D.; W7-X Team. Numerical simulation of neutral gas dynamics in the W7-X sub-divertor. *Nucl. Fusion* **2024**, *64*, 076011. [CrossRef]
19. Kallenbach, A.; Bernert, M.; Beurskens, M.; Casali, L.; Dunne, M.; Eich, T.; Giannone, L.; Herrmann, A.; Maraschek, M.; Potzel, S.; et al. Partial detachment of high power discharges in ASDEX Upgrade. *Nucl. Fusion* **2015**, *55*, 053026. [CrossRef]
20. Sun, G.; Reimerdes, H.; Theiler, C.; Duval, B.P.; Carpita, M.; Colandrea, C.; Ducker, R.; Février, O.; Gorno, S.; Simons, L.; et al. Investigating the influence of divertor baffles on nitrogen-seeded detachment in TCV with SOLPS-ITER simulations and TCV experiments. *Nucl. Fusion* **2025**, *65*, 026061. [CrossRef]
21. Haak, V.; Bozhenkov, S.A.; Feng, Y.; Kharwandikar, A.; Kremeyer, T.; Naujoks, D.; Perseo, V.; Schlisio, G.; Wenzel, U. Overview over the neutral gas pressures in Wendelstein 7-X during divertor operation under boronized wall conditions. *Plasma Phys. Control. Fusion* **2023**, *65*, 055024. [CrossRef]
22. Yagasaki, K.; Okamoto, A.; Sugimoto, M.; Higuchi, S.; Koike, M.; Sato, K.; Yamada, Y.; Fujita, T. Development of a simple calculation method for the conductance of rarefied gas flow in cylindrical pipe applicable to divertor exhaust investigation of nuclear fusion reactor. *J. Nucl. Sci. Technol.* **2024**, *61*, 1431–1437. [CrossRef]
23. Hauer, V.; Day, C. Conductance modelling of ITER vacuum systems. *Fusion Eng. Des.* **2009**, *84*, 903–907. [CrossRef]
24. Hauer, V.; Day, C. ITER divertor gas flow modelling. *Fusion Eng. Des.* **2015**, *98–99*, 1775–1778. [CrossRef]
25. Vasileiadis, N.; Tatsios, G.; Misdanitis, S.; Valougeorgis, D. Modeling of complex gas distribution systems operating under any vacuum conditions: Simulations of the ITER divertor pumping system. *Fusion Eng. Des.* **2016**, *103*, 125–135. [CrossRef]
26. Vasileiadis, N.; Valougeorgis, D. Modeling of time-dependent gas pumping networks in the whole range of the Knudsen number: Simulation of the ITER dwell phase. *Fusion Eng. Des.* **2020**, *151*, 111383. [CrossRef]
27. Ehrke, G. Design and manufacturing of the Wendelstein 7-X cryo-vacuum. *Fusion Eng. Des.* **2019**, *146*, 2757. [CrossRef]
28. SALOME PLATFORM—The Open-Source Platform for Numerical Simulation. Available online: https://www.salome-platform.org/ (accessed on 20 August 2025).

29. Wadsworth, D.C.; Erwin, D.A. Numerical simulation of rarefied flow through a slit. Part I: Direct simulation Monte Carlo results. *Phys. Fluids A* **1993**, *5*, 235–242. [CrossRef]
30. Fujimoto, T.; Usami, M. Rarefied Gas Flow Through a Circular Orifice and Short Tubes. *J. Fluids Eng.* **1984**, *106*, 367–373. [CrossRef]
31. Yoshida, H. Upgrading of the modified Knudsen equation and its verification for calculating the gas flow rate through cylindrical tubes. *J. Vac. Sci. Technol. A* **2024**, *42*, 044201. [CrossRef]
32. Varoutis, S.; Valougeorgis, D.; Sharipov, F. Simulation of gas flow through tubes of finite length over the whole range of rarefaction for various pressure drop ratios. *J. Vac. Sci. Technol. A* **2009**, *27*, 1377–1391. [CrossRef]

Disclaimer/Publisher's Note: The statements, opinions and data contained in all publications are solely those of the individual author(s) and contributor(s) and not of MDPI and/or the editor(s). MDPI and/or the editor(s) disclaim responsibility for any injury to people or property resulting from any ideas, methods, instructions or products referred to in the content.